



 Cite this: *RSC Adv.*, 2018, 8, 25754

Three-dimensional mesoporous calcium carbonate–silica frameworks thermally activated from porous fossil bryophyte: adsorption studies for heavy metal uptake

 Wenlei Wang, * Ren He, Tianli Yang, Yunchu Hu, Ning Zhang and Can Yang

In this paper, three-dimensional mesoporous calcium carbonate–silica frameworks have been created from the straw tufa (ST) originating from porous fossil bryophyte by a thermal activation technique. A batch of adsorption kinetic and thermodynamic experiments were used to investigate the adsorption capacity of Cd(II) onto the samples. The ST after thermal activation has shown a significant ability for the uptake of heavy metals. It exhibited maximum adsorption capacities of 12.76 mg g^{−1}, 14.09 mg g^{−1}, 17.00 mg g^{−1}, and 33.81 mg g^{−1} for Cd(II) at the activation temperature of 300, 450, 600 and 750 °C, respectively. Through competitive adsorption for Cd(II) and Pb(II), the ST thermally activated at 750 °C exhibited maximum equilibrium adsorption capacities of 24.65 mg g^{−1}, 25.91 mg g^{−1}, and 30.94 mg g^{−1} for Cd(II) uptake at 298.1 K, 308.1 K and 318.1 K, respectively, whereas it exhibited values of 91.59 mg g^{−1}, 101.32 mg g^{−1}, and 112.19 mg g^{−1} for Pb(II) removal. The adsorption capacities of Cd(II) and Pb(II) both decrease with the addition of the other heavy metal cations, indicating that the adsorption is hindered by the competitive adsorption and the adsorption active sites on the mineral surface are readily exchangeable. The adsorption of Cd(II) and Pb(II) followed the pseudo-second order kinetics model well. In addition, the Langmuir model could accurately describe the adsorption isotherms. Based on the results of characterization with TEM, XRD and XPS, the adsorption mechanisms could be primarily explained as formation of Cd(OH)₂ and CdCO₃ as well as Cd(HCO₃)₂ precipitation on the surface of ST. These characteristics of ion-exchange and the adsorptive property for ST modified allow it to be widely used in artificial wetland landfill and environmental protection.

Received 6th June 2018

Accepted 12th July 2018

DOI: 10.1039/c8ra04825h

rsc.li/rsc-advances

1. Introduction

Though emissions of heavy metals into water and soil ecosystems have declined in most countries over the last decades, the danger of heavy metals to health continues and is even increasing in some parts of the world because products containing heavy metals are rarely recycled and are dumped together with household waste without any treatment.^{1–3} The main threats to human health from heavy metals are associated with exposure to Cd(II) and Pb(II).^{4–7} Several typical techniques have been applied for heavy metal removal from aqueous solutions to minimize the risk of adverse health effects, such as hydroxide precipitation method,^{8–10} ferrite reaction separation,¹¹ ion exchange method,^{12–15} and membrane treatment technology.^{16–19} Among these options, increasing attention has been paid to adsorption due to its economic feasibility, effectiveness, simplicity of application, and environmental friendliness.^{20–25} The adsorbent was the key parameter for the adsorption process of heavy metals.^{26,27} Carbonates, common

minerals in soils and sediments, show a significant ability for the uptake of divalent metals.^{28,29} In addition to the low-cost adsorbents, materials such as zeolites, activated carbons, clays and biochars were used for heavy metal removal.^{30–32} Especially, natural minerals with mesoporous structures may have more potential to be applied in the treatment of heavy metals.^{33–35} Straw tufa (ST) is abundant and is essentially fossilized calcium carbonate bryophyte formed approximately 130 million to 190 million years ago. Most structures have unique porous characteristics with tubular and hollow features. The tubes are gradually formed by continuous corrosion and alternations in the process of generation due to the features of fossilized plant matter, such as stems, leaves, weeds, *etc.* It has great potential to be applied in the treatment of heavy metals of Cd(II) and Pb(II) in the environment.

In this paper, Brunauer–Emmett–Teller (BET) and thermogravimetric analysis-differential scanning calorimetry (TG-DSC) were applied to determine the mesoporous feature and decomposition temperature on the natural carbonate ore of ST. A thermal activation is applied to modify the structural characteristics and get optimal adsorption activity of the adsorbent sample. The structural properties of the ST samples after

College of Science, Central South University of Forestry and Technology, Changsha 410004, P. R. China. E-mail: wenlei_wang@hotmail.com



thermal activation are characterized by Fourier transform infrared spectroscopy (FT-IR), X-ray diffraction (XRD), and scanning electron microscope (SEM). Then, the efficiency of ST before and after thermal activation for the uptake of Cd(II) and Pb(II) was systematically investigated. Based on the newly obtained experimental data of the adsorption kinetics, several kinetic models were applied to evaluate the interaction of heavy metal cations of Cd(II) and Pb(II) with ST as an adsorbent. Additionally, Langmuir and Freundlich models were used to evaluate the experimental data of the adsorption isotherms to help understand the adsorption mechanism. The adsorption mechanism of Cd(II) onto the ST sample was studied by using XRD, Transmission electron microscopy (TEM), and X-ray photoelectron spectroscopy (XPS). The results of this work will help to understand the adsorption properties of the ST on *in situ* curing and removal of cadmium ions as well as other heavy metal ions.

2. Materials and methods

2.1. Materials and chemical reagents

The natural porous material of ST was obtained from Linqu County, Shandong province, China. All reagents ($\text{Cd}(\text{NO}_3)_2 \cdot 4\text{H}_2\text{O}$ and $\text{Pb}(\text{NO}_3)_2$) used in this work were analytical grade chemicals purchased from Sinopharm Chemical Reagent Co., Ltd, China. Then, $\text{Cd}(\text{NO}_3)_2$ and $\text{Pb}(\text{NO}_3)_2$ were purified two times by crystallization with half salt recovery of the analytical grade reagent in each case, as discussed in our previous work.³⁶ The Cd(II) and Pb(II) stock aqueous solutions were prepared with the newly obtained chemical agents mentioned above. Doubly distilled water with $S < 1.5 \times 10^{-4} \text{ S m}^{-1}$ was used in the adsorption experiment. A thermostat (Lauda E219, Germany) with a temperature stability up to $\pm 0.01 \text{ K}$ was used to perform the kinetic and equilibrium experiments with the bath temperature determined by a calibrated glass thermometer (Miller & Weber, Inc., USA). The Cd(II) and Pb(II) analyses were performed by the standard addition method with an inductively coupled plasma optical emission spectrometer (ICP-OES) (5300DV, Perkin-Elmer, USA).

2.2. Physical and chemical properties of the sample

The composition of ST was evaluated by X-ray fluorescence (XRF) (PANalytical-Axios). To measure the textural properties of the sample, including the surface area, pore volume, and average pore diameter, N_2 adsorption-desorption isotherms were performed on a Coulter Omnisorp 100CX Brunauer-Emmett-Teller (BET) system. Simultaneous thermogravimetric (TG) and differential scanning calorimetric (DSC) measurements, TG-DSC was performed using a Netzsch STA 449C Jupiter system. Samples of approximately 200 mg were determined from 20 to 900 °C. The functional groups on the sample surface were characterized with Fourier transform infrared spectrometry (FT-IR) (Thermo Scientific Nicolet-iS10, USA) by the KBr pressed disk technique. The FT-IR spectrum was recorded at 32 scans per spectrum with a resolution of 0.1 cm^{-1} from wave numbers 400–4000 cm^{-1} . The ratio of sorbent to KBr

was 0.5 : 100. XRD patterns were collected on a Bruker D8 Advanced X-ray diffractometer with Cu K α radiation at 40 kV and 40 mA. The adsorbent was scanned with a speed of 5° per min over a scanning range of 10–90°. Measurements on high-resolution SEM/EDS systems equipped with a transmission model for imaging and measurement of the morphology of the samples were performed on a field emission scanning electron microscope (FE-SEM) (Ultra 55, Germany). In order to investigate the adsorption mechanism onto the ST before and after adsorption, the microstructure and the element distribution of the adsorbent material was analyzed by the transmission electron microscope (HR-TEM) (Tecnai G2 F20 S-TWIN). X-ray photoelectron spectroscopy (XPS) analyses were performed with an Axis Ultra spectrometer (Kratos Analytical Ltd.) using Al monochromatic X-ray source (Al K α = 1486.6 eV) at 25 °C in a high vacuum environment (approximately 5×10^{-9} torr) with the binding energies calibrated with containment carbon the C 1s (284.8 eV).

2.3. Thermal activation

In order to modify the characteristic properties and increase the specific surface area of ST, the ST needs to be treated by using a thermal activation technique. Preparation of three-dimensional mesoporous calcium carbonate-silica frameworks was performed from a step of slow pyrogenic decomposition followed by physical activation with CO_2 . Amounts of 2.0 g of the precursor material was introduced into a stainless steel reactor with a volume of 20 mL and removable lid with orifices for gas inlet, which was heated in a vacuum tube furnace (KJ-T1400-L6008LB2, China) with a temperature program of three stages. The very beginning, the sample was heated with a heating rate of 30 °C min^{-1} to a prescribed temperature such as 300, 450, 600 and 750 °C, and then was held the prescribed temperature for 1 h under N_2 flow of 100 mL min^{-1} . Then, the temperature was increased to a aimed temperature and maintained for 2 h. Afterwards, the crucible with the sample was removed from the vacuum tube furnace when it dropped to room temperature. Ultimately, the thermal activated ST was obtained and abbreviated as ST-T, where the T was the above prescribed temperature.

2.4. Batch adsorption experiments

Cd(II) was selected as representative pollutants to investigate the adsorption properties of the thermal activated ST. A batch of experiments have been carried out on adsorption kinetics and adsorption thermodynamics. Cd(II) adsorption kinetics experiments were evaluated with 50 mL of 150 mg L^{-1} Cd^{2+} solution in a 150 mL Erlenmeyer flask at 298.1 K. The Erlenmeyer flask was shaken on a thermostat shaker (Lauda E219, Germany) under 150 rpm min^{-1} . The experiments with 0.2 g adsorbent including ST and ST-750 were used for performing the adsorption kinetic. Samples were withdrawn from the flask at pre-determined time intervals and immediately filtered by 0.45 μm membrane filters prior to further analysis. Then, the Cd(II) concentration of the samples was measured by ICP-OES. Then, adsorption isotherms of Cd(II) were carried out by a batch of



equilibration experiments. To evaluate the influences of initial Cd(II) concentration and the thermal activation temperature, the adsorption equilibrium experiments were carried out in a 150 mL Erlenmeyer flask containing 50 mL of Cd(II) aqueous solution (50, 100, 150, and 200 mg L⁻¹) and 0.2 g adsorbents including ST, ST-300, ST-450, ST-600, and ST-750. The Erlenmeyer flasks were shaken for 12 h in a thermostat at 298.1 K with temperature stability up to ± 0.1 K. The pH value of the reaction solution was maintained at 6 for subsequent adsorption experiments. The supernatants were collected to determine the equilibrium Cd(II) concentrations by a syringe with 0.45 μ m membrane filters.

The competitive adsorption experiments in contact with Cd(II) and Pb(II) were conducted in controlled aqueous systems. 50 mL of Cd(II) and Pb(II) stock aqueous solutions were transferred into a ground 150 cm³ Erlenmeyer flask at $T = 298.1$, 308.1 and 318.1 K. The content of the aqueous solution was set to a standard value by diluting the above stock solutions. Then, 0.2 g of ST-750 was added as an adsorbent to the reaction aqueous solution. The adsorption sample was placed into a glycol-water bath thermostat and stirred by a magnetic stirrer at 150 rpm outside the bath. The adsorption kinetics experiments were conducted at predetermined times of 5, 15, 30, 45, 60, 90, 120, 300, 720, 900, and 1440 min with the initial Cd(II) and Pb(II) concentrations set at 100 mg L⁻¹ and 400 mg L⁻¹, respectively. The adsorption isotherm experiments were performed with initial Cd(II) concentrations of 5, 10, 15, 25, 50, 80, 100, 150, 200 mg L⁻¹ and Pb(II) concentrations of 10, 25, 50, 100, 200, 400, 600, 800, 1000 mg L⁻¹, respectively. The relative metal ion concentration of the aqueous solution in contact with ST-750 were sampled and measured at regular time intervals. A syringe filter with a 0.45 μ m pore size membrane was used to filter the suspensions after adsorption. The removed sample solution was diluted with distilled water. The aqueous solutions in each flask with Cd(II) and Pb(II) concentrations were mixed well by shaking and analyzed by ICP-OES.

2.5. Data analysis

2.5.1. Adsorption kinetics. The adsorption capacity (q_t) of ST before and after thermal activation for Cd(II) and Pb(II) uptake was calculated by the following equation:

$$q_t = (C_0 - C_t)V/m \quad (1)$$

where q_t was the amount of heavy metal cations adsorbed (mg g⁻¹) at any time t (min). C_0 and C_t (mg L⁻¹) were the initial and remaining Cd(II) and Pb(II) concentrations, respectively. V (L) was the volume of the suspension; m (g) was the adsorption capacity of heavy metals.

The experimental data were described by the widely used pseudo-first order and pseudo-second order models, which are generally expressed as follows:

$$q_t = q_e(1 - e^{-k_1 t}) \text{ (pseudo-first order equation)} \quad (2)$$

$$q_e = \frac{q_e^2 k_2 t}{1 + q_e k_2 t} \text{ (pseudo-second order equation)} \quad (3)$$

The linear form of the pseudo-second order equation can be described as:

$$\frac{t}{q_t} = \frac{1}{k_2 q_e^2} + \frac{t}{q_e} \quad (4)$$

where q_e was the amount of Cd(II) or Pb(II) adsorbed (mg g⁻¹) at equilibrium, and k_1 was the rate constant of pseudo-first-order kinetics model accompanying the physical quantity unit of min⁻¹. k_2 was the rate constant of pseudo-second-order kinetics model accompanying a physical quantity unit of g mg⁻¹ min⁻¹.

To determine whether intra-particle diffusion was the rate-limiting step of adsorption for heavy metal cations, the intra-particle diffusion model was suggested. It can be expressed as follows:

$$q_t = K_{id} t^{0.5} + C \text{ (intra-particle diffusion model)} \quad (5)$$

where k_{id} is the intraparticle diffusion rate constant (mg (g min^{0.5})⁻¹). C is a constant related to the boundary layer thickness.

2.5.2. Adsorption isotherm. Adsorption isotherms were fitted using the Langmuir and Freundlich models.

Langmuir model:

$$q_e = \frac{q_{\max} K_L C_e}{1 + K_L C_e} \quad (6)$$

The linear forms of the Langmuir model can be described as:

$$\frac{C_e}{q_e} = \frac{1}{K_L q_{\max}} + \frac{C_e}{q_{\max}} \quad (7)$$

where C_e (mg L⁻¹) represents the equilibrium concentration of Cd(II) and Pb(II) in the aqueous solutions, K_L (L mg⁻¹) represents the Langmuir adsorption affinity parameter, while q_e and q_{\max} (mg g⁻¹) represent the equilibrium adsorption capacity and maximum adsorption capacity, respectively.

Freundlich model:

$$q_e = K_F C_e^{1/n} \quad (8)$$

The linear forms of the Freundlich model can be described as:

$$\log q_e = \log K_F + \frac{1}{n} \times \log C_e \quad (9)$$

where K_F (mg g⁻¹ (mg L⁻¹)^{-1/n}) is the Freundlich distribution coefficient, and $1/n$ is empirical constant of the Freundlich describing the adsorption intensity or surface heterogeneity.

3. Results and discussion

3.1. Properties of straw tufa

The composition of the natural ST was evaluated by XRF. The results were listed in Table 1. It is mainly composed of Ca, Si, Al and Fe. Its Ca, Si, Al, and Fe contents were 53.49%, 12.51%, 3.80% and 3.91%, respectively. However, much lower K, Ti and



Table 1 Composition of ST

Sample	Ca	Si	Al	Fe	K	Ti	Sr
Wt/%	53.491	12.507	3.804	3.922	1.031	0.751	0.235

Sr contents were found in the ST with values of 1.03%, 0.75% and 0.24%, respectively.

The N₂ adsorption–desorption isotherm and BJH adsorption pore size distributions of the natural ST were explored. Fig. 1(a)

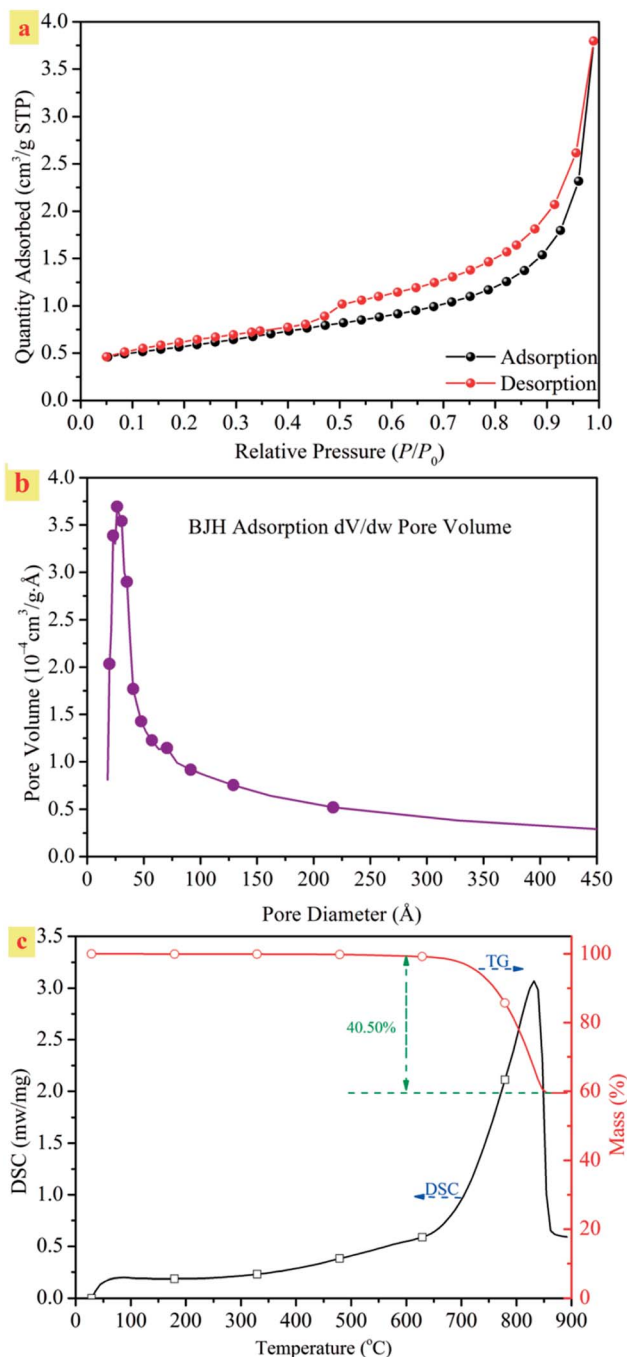


Fig. 1 (a) BET surface area plot. (b) Pore size distribution. (c) TG-DSC profiles obtained for ST.

shows the N₂ adsorption–desorption isotherms of the sample. The ST belonged to the typical type IV of adsorption isotherms with a H1 hysteresis loop, which is characteristic of mesoporous structures. The steepness of the capillary condensation step suggested the presence of mesopores, which was further confirmed by the pore size distribution shown in the inset of Fig. 1(b). The desorption isotherm was at the top of the adsorption isotherm, accompanied by producing adsorption hysteresis. The ST was mesoporous with a large specific surface area of 427.0 m² g⁻¹ and a pore diameter of 11.77 nm. The natural mesoporous structures form a basis of a high efficiency for the uptake of heavy metal cations by the ST and allow a direct water discharge after metal removal without any other treatment.

The TG-DSC technique was used to investigate the thermal behavior of ST, which could provide the necessary data for the following decomposition process. Fig. 1(c) shows the typical TG-DSC curves of the natural straw tufa. As shown in the DSC curve, a broad endothermic peak from 650 to 850 °C involved the decomposition reaction of carbonate ores. An endothermic peak was centered at 829 °C for the ST. The endothermic peak demonstrated a phase change, indicating the formation of a new mineral. In addition, an obvious weight loss peak appeared from 700 °C in the TG curve. The breaking up of the crystal lattice was accompanied by a 40% weight loss due to the decomposition reaction of calcite with CO₂ releasing.

3.2. Properties of ST after thermal activation

Fig. 2(a) presents the functional groups of ST. The adsorption bands appearing at 1390 cm⁻¹ and 1792 cm⁻¹ were associated with the C–O stretching vibration band and C–O antisymmetric stretching vibration, respectively. The CO₃²⁻ external deformation vibration peak was observed at a frequency of 876 cm⁻¹. The 1003 cm⁻¹ peak was associated with Si–O deformation vibration in plane referred to SiO₃²⁻. It indicated that the ST before and after thermal activation has no obvious change. X-ray diffraction (XRD) was used to characterize the phase composition of ST, ST-600 and ST-750. As shown in Fig. 2(b), there was little obvious change on the diffraction peaks of the ST before and after thermal activated, indicating that the composition of the sample before and after thermal activated has no significant change. A part of the sample belongs to calcite with the similar diffraction peaks related to the (012), (104), (006), (110), (113), (202), (018), (024), (112), (119) and (300) planes (PDF 05-0586[#]). The other part of the sample belongs to SiO₂ with the analogical diffraction peaks related to the (100) and (011) planes (PDF 85-0794[#]). As you see, ST was primarily composed of calcite and SiO₂, which was also supported by the result of XRF.

Fig. 3 presents the SEM photographs of the ST before and after thermal activation. As illustrated in Fig. 3(a), the spatial structure of the ST shows a three-dimensional reticulate structure. There are interconnected caves and drill ways in the cage construction. This might be the main reason for that water absorption for ST is very strong. As shown in Fig. 3(b), the fossilized features of calcium carbonate bryophyte can be



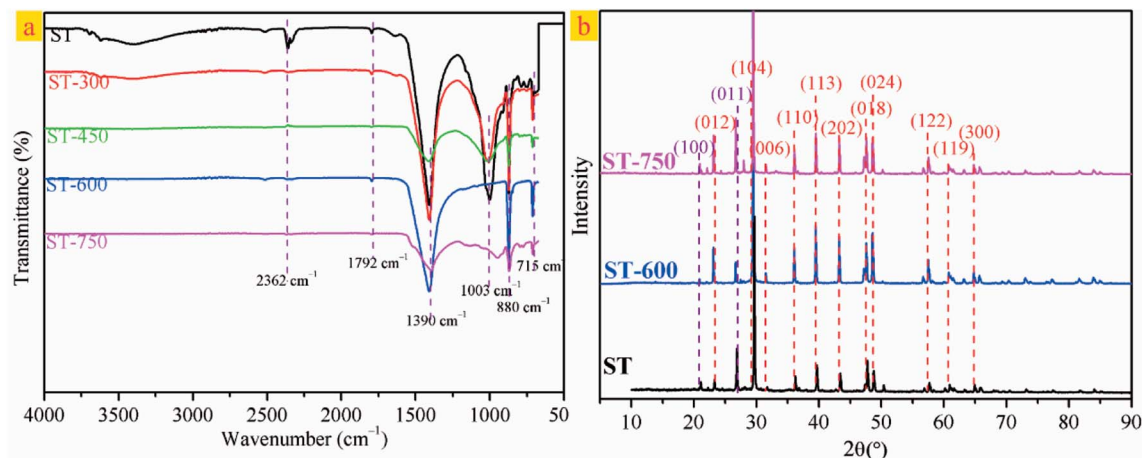


Fig. 2 (a) FT-IR spectra for ST, ST-300, ST-450, ST-600 and ST-750. (b) XRD profiles obtained for ST, ST-600 and ST-750.

clearly reflected on the pore wall of the interconnected caves and drill ways. After thermal activation at 300 and 450 $^{\circ}\text{C}$, the coralliform and perforated structure of the sample could be seen clearly, (see Fig. 3(c) and (d)). The interconnected caves and drill ways are connected to each other through openings, effectively increasing the specific surface area with cave effects. As can be seen in Fig. 3(e), the phenomenon is more pronounced with increasing the thermal activation temperature up to 600 $^{\circ}\text{C}$. Most of the surface has collapsed and the edge of the pore began to collapse. To move forward a single step, the pore aperture of the sample has been enlarged to approximately 2 μm and the edge of the pore continues to collapse with continuously increasing the thermal activation temperature to 750 $^{\circ}\text{C}$, as seen in Fig. 3(f). Three-dimensional mesoporous calcium carbonate–silica frameworks, which could be described a coralliform and perforated structure, have been successfully synthesized from porous fossil bryophyte by the thermally activation technique. These porous structural features could

lead to a selective adsorption capacity of a molecular sieve and strong super-pore effects, and effectively increase the surface area and enhance the adsorption activity site. In addition, the mesoporous molecular structure forms a large electrostatic attraction accompanied by a considerable degree of stress. The internal stress will give rise to a preferential adsorption of heavy metal ions that is selective and efficient.

3.3. Adsorption kinetics

To understand the dynamic interaction of the heavy metal cations of Cd(II) with the ST before and after thermal activation, and to predict the time required for adsorption equilibrium, ST and ST-750 were added as initial solid adsorbent into an aqueous solution with a known Cd(II) concentration at 298.1 K. Then, the metal cation concentration in the aqueous solution was measured by ICP-OES at regular intervals. The experimental amounts of Cd(II) adsorbed over time are plotted in Fig. (4),

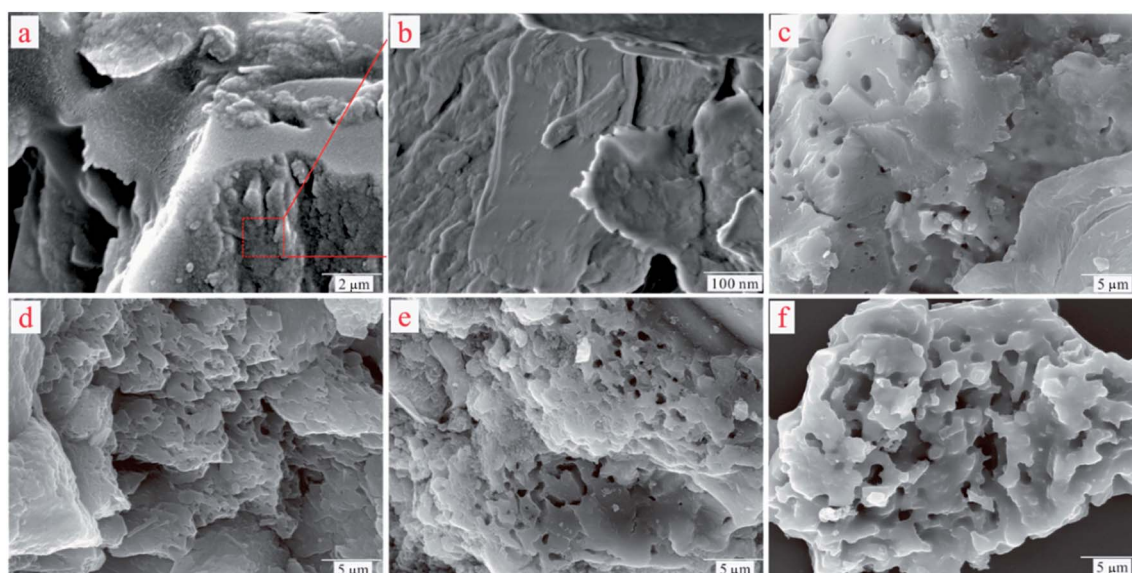


Fig. 3 (a) SEM images of ST. (b) Magnified view of the red square region in (a). (c) SEM image of ST-300. (d) SEM image of ST-450. (e) SEM image of ST-600. (f) SEM image of ST-750.



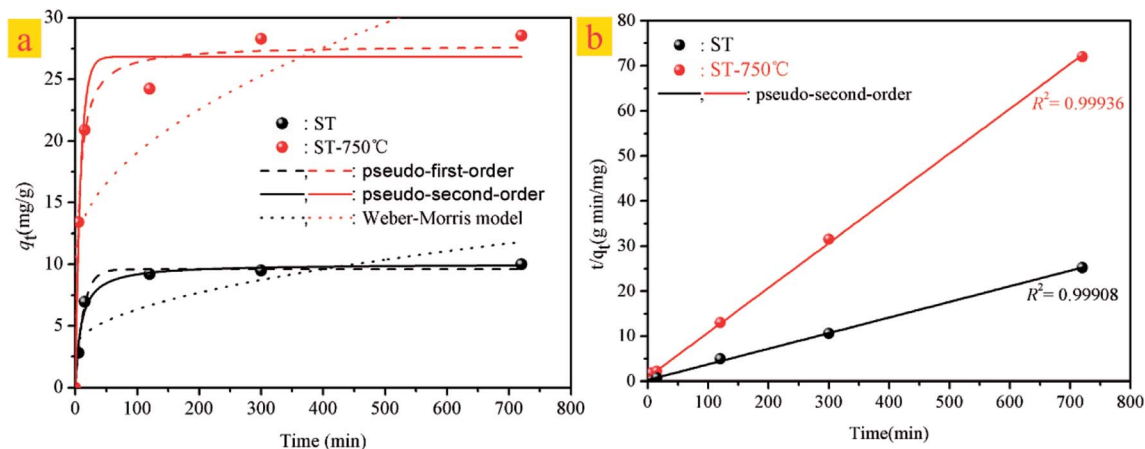


Fig. 4 (a) Kinetic models for Cd(II) adsorption on ST and ST-750. (b) The linear analysis of pseudo-second-order kinetics model for Cd(II) adsorption on ST and ST-750.

which presents the influence of reaction time on the adsorption rate of Cd(II) with the ST and ST-750 as the adsorbent. The Cd(II) adsorption amount on ST and ST-750 reached 10.05 mg g^{-1} and 28.55 mg g^{-1} . The Cd(II) concentration in the aqueous solution first sharply increases in the first 100 min step before reaching adsorption equilibrium. Then, it is followed by a relatively slower increase. The drastically increasing section of the adsorption can be understood as a result of the sufficient active adsorption sites on the ST and ST-750 interface exposed to Cd(II) at the beginning of each experiment, and the decreasing section of adsorption can be interpreted as that of active adsorption sites taken up as time goes on. The decreasing section of adsorption can also be attributed to the decrease of the BET surface area, which is consistent with the increasing average pore diameter of the ST during the demineralization process. This may be caused by the removal of minerals incorporating K and Sr and the enlargement of the pores existing in the natural porous structure, resulting in the pore diameter increasing and ash content decreasing. This finding indicates that relatively less polar functional groups and less aromatic structures are present. The highest concentrations detected during each experimental process could be assigned as the equilibrium adsorption capacity of the initial solid phase in this work. It is obvious that a duration of at least 100 min was needed for the aqueous solution of Cd(II) with ST and ST-750 to reach adsorption equilibrium if ST and ST-750 were added to the solution as the initial solid phase in a 100 mg L^{-1} Cd(II) aqueous solution.

Furthermore, the kinetic mechanism of Cd(II) adsorption with the ST and ST-750 as adsorbent also followed the pseudo

first-order kinetic model and pseudo second-order kinetic model, as described in eqn (2) and (3). The predicted fitting curves of the two kinetic models are plotted in Fig. 4(a), with the dashed lines calculated from the pseudo first-order kinetic model and the solid lines calculated from the pseudo second-order kinetic model. The relevant parameters of the pseudo first-order kinetic model and pseudo second-order kinetic model are tabulated in Table 2. According to the correlation coefficient value R^2 , the experimental data of Cd(II) adsorption were better fitted by the pseudo second-order kinetic model because of a higher value of R^2 .

In addition, the pseudo-second-order adsorption kinetics model estimated *via* linear analysis using eqn (4) was shown in Fig. 4(b). It can be found that the calculated values for the equilibrium adsorption capacity predicted by the pseudo second-order kinetics model possessed a high consistence with the experimental values. The R^2 of linear form of pseudo-second-order adsorption kinetics model is 0.9830 and 0.9841 for ST and ST-750, respectively. Therefore, the pseudo second-order kinetic model was used to evaluate the whole adsorption equilibrium process. In regard to these two kinetic models, it can be noted that the pseudo first-order kinetic model views the rate of occupation of the adsorption active sites to be proportional to the number of unoccupied sites, while the pseudo second-order kinetic model depicts the rate limiting step as the formation of a chemisorptive bond involving valence forces, namely, the sharing or exchange of electrons between the sorbent and sorbate. Obviously, the agreement of the predicted and experimental data for adsorption of Cd(II) shows the adsorption of Cd(II) with ST and ST-750 as the adsorbent occurs

Table 2 Kinetic parameters for Cd(II) adsorption on ST and ST-750

Adsorbent	Pseudo-first order model			Pseudo-second order model			Weber-Morris model		
	$q_e (\text{mg g}^{-1})$	$k_1 (\text{min}^{-1})$	R^2	$q_e (\text{mg g}^{-1})$	$k_2 (\text{g mg}^{-1} \text{min}^{-1})$	R^2	$K_{id} (\text{mg g}^{-1} \text{min}^{-0.5})$	C	R^2
ST	9.59	0.07971	0.9923	10.02	0.0108	0.9830	0.3260	3.0824	0.5903
ST-750	26.83	0.1196	0.9674	27.78	0.00674	0.9841	0.8506	10.5554	0.5558



by chemical adsorption, and the rate limiting step stems from the conjugation between the ST before and after thermal activation and heavy metal cations. As shown in Fig. 4(a), the intra-particle diffusion model was also used to evaluate the dynamic interaction of the heavy metal cations Cd(II) with ST and ST-750 as the adsorbent by using eqn (5). According to the intra-particle diffusion model, if the rate limiting step is the intra-particle diffusion, the q_t plotted against the square root of time should be a straight line and pass through the origin ($C = 0$), the deviation of the plot from the linearity indicates that the rate-limiting step should be boundary layer (film) diffusion. As can be seen in Fig. 4(a), the calculation result indicates that the intra-particle diffusion is not the rate limiting step and the rate limiting step is the formation of chemisorptive bond involving valence forces.

3.4. Adsorption isotherm

Adsorption isotherms were performed to evaluate the adsorption performance of the ST before and after thermal activation in contact with Cd(II) at $T = 298.1$ K, through which the relationship between adsorbent concentration and the adsorption capacity was further investigated. The adsorption isotherms of Cd(II) onto ST, ST-300, ST-450, ST-600, and ST-750 are shown in Fig. (5). To construct the adsorption capacity regions of Cd(II) as a function of activation temperature and initial equilibrium concentration, an adsorption mechanism model is necessary to simulate and predict the adsorption properties of ST, ST-300, ST-450, ST-600 and ST-750. As discussed in previous studies, the widely used Langmuir and Freundlich models are sufficient for this task. Then, the experimental data were calculated by using eqn (6) and (8) of the Langmuir and Freundlich models, with the calculated results plotted in Fig. (5) and with the model parameters tabulated in Table 3. Applying the model parameters in Table 3, we predicted the adsorption isotherms of Cd(II) with ST, ST-300, ST-450, ST-600 and ST-750 as the adsorbent in the aqueous solution. The calculated results from Freundlich model deviate largely from our experimental data of adsorption capacity. The calculated results from Langmuir model are highly consistent with our experimental data for the adsorption capacity. The Langmuir model is apparently necessary to describe the properties of the system.

The adsorption capacity of Cd(II) in the aqueous solution during the adsorption process as a function of aqueous equilibrium concentration is presented in Fig. 5. As illustrated, the adsorption capacity of Cd(II) with ST before and after thermal activation as the adsorbent increased drastically at first and then remained unchanged. In Cd(II) aqueous solution at 298.1 K, the equilibrium adsorption capacity q_e increases with the aqueous equilibrium concentration of Cd(II) increasing. A comparison of the correlation coefficients (R^2 , Table 4) indicates that the adsorption of Cd(II) onto ST, ST-300, ST-450, ST-600, and ST-750 can be well fit using a Langmuir model with a correlation coefficient of 0.9740, 0.9773, 0.9915, 0.9978, and 0.9297. As illustrated by the constant values in the Langmuir model, the maximum adsorption capacity (q_{\max}) value of Cd(II) adsorbed onto ST, ST-300, ST-450, ST-600, ST-750 were 14.05 mg

g^{-1} , 12.76 mg g^{-1} , 14.09 mg g^{-1} , 17.00 mg g^{-1} and 33.81 mg g^{-1} respectively. Previous studies have demonstrated that the natural calcium carbonate had a low adsorption capacity of 18.52 mg g^{-1} for Cd^{2+} .³⁷ Thermal activated serpentine at 700 °C exhibited a maximum adsorption capacity of 15.21 mg g^{-1} for

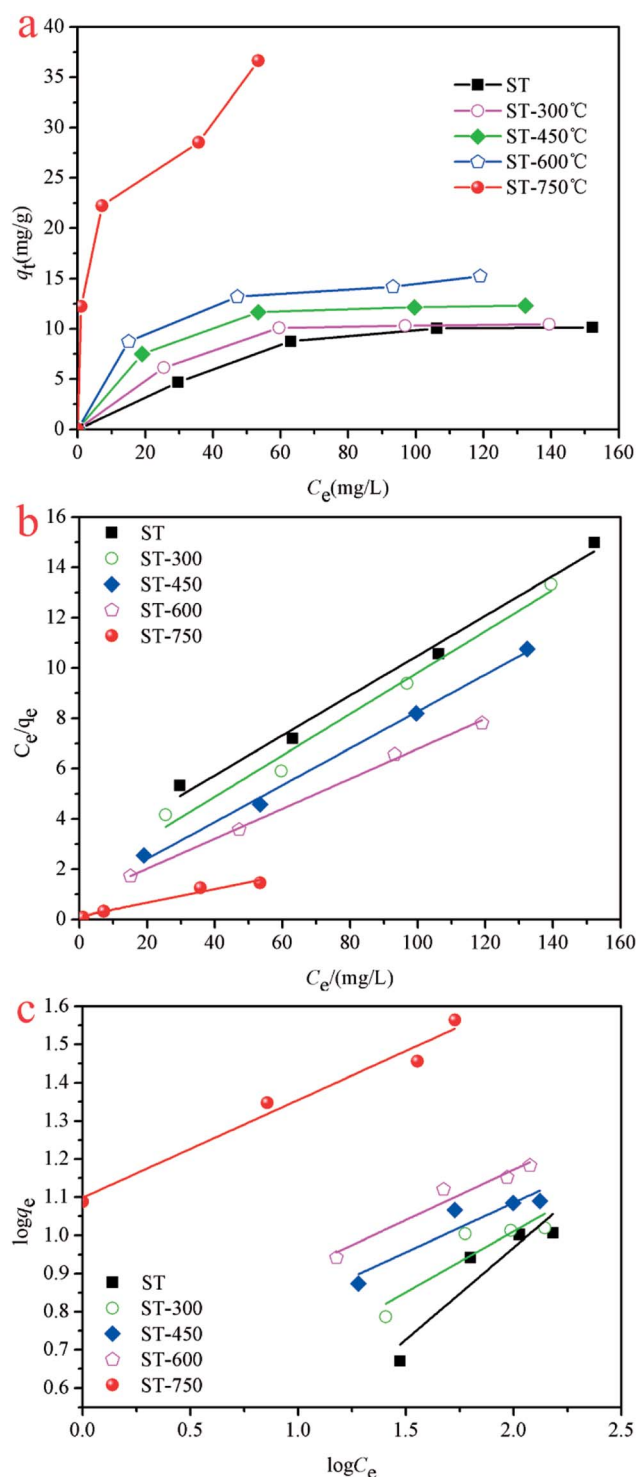


Fig. 5 (a) Isotherms of Cd(II) adsorption on ST and ST-T as a function of temperature. (b) Linear fitting curves with Langmuir model on ST and ST-T. (c) Linear fitting curves with Freundlich model on ST and ST-T.



Table 3 Langmuir and Freundlich isotherm model parameters for adsorption of Cd(II) on ST

Adsorbent	Langmuir isotherm			Freundlich isotherm		
	q_{\max} (mg g ⁻¹)	K_L (L mg ⁻¹)	R^2	K_F (L mg ⁻¹)	n	R^2
ST	14.05	0.02091	0.9740	1.4746	0.3981	0.9459
ST-300	12.76	0.04283	0.9773	2.8979	0.2724	0.9525
ST-450	14.09	0.0654	0.9915	4.1547	0.2317	0.9717
ST-600	17.00	0.0737	0.9978	4.7244	0.2474	0.9893
ST-750	33.81	0.3975	0.9297	12.6689	0.2536	0.9775

Table 4 Isotherm parameters of Cd(II) adsorption Pb(II) adsorption by ST-750 at 298.1 K, 308.1 K, 318.1 K

Metal ions	Temp. (K)	Langmuir parameters			Freundlich parameters		
		$q_{\max}/\text{mg g}^{-1}$	$K_L/\text{L mg}^{-1}$	R^2	$1/n$	k	R^2
Cd(II)	298.1 K	33.81	0.3973	0.9297	12.6689	0.9775	33.8128
	308.1 K	35.11	1.5013	0.9720	18.4958	0.9738	35.1115
	318.1 K	36.91	1.8888	0.9904	21.3997	0.9569	36.9088
Pb(II)	298.1 K	91.64	0.2469	0.9562	36.8619	0.8689	91.6399
	308.1 K	100.74	0.2128	0.9644	34.4626	0.8816	100.7412
	318.1 K	110.25	0.2134	0.9559	36.8237	0.8757	110.2463

Cd²⁺ removal.³⁸ In comparison, the straw tufa modified allows it to be widely used in artificial wetland landfill and environmental protection. Furthermore, the adsorption isotherm model for the adsorption of Cd(II) on different ST samples estimated *via* linear analysis of the data using eqn (7) and (9) were shown in Fig. 5(b) and (c). It is clearly observed that the Langmuir model was more suitable for describing the adsorption behavior of Cd(II) on the adsorbents than the Freundlich model. All samples showed the same trends. This phenomenon occurs because there are many more occupied active adsorption sites in low Cd(II) initial concentration aqueous solution, while fewer occupied active adsorption due to active adsorption sites that existed in the high Cd(II) initial concentration aqueous solution when active adsorption sites were saturated by Cd(II) up to equilibrium. With an increase in temperature, the maximum adsorption capacity q_{\max} required for complete adsorption increases.

The major difference in adsorption capacity implies that ST after thermal activation was an excellent adsorption material, possessing high adsorption efficiency towards template ions. In addition, these curves depicted that the saturated adsorption capacity increased with increasing temperature. The adsorption capacity changes can be explained since the ST before and after thermal activation was a temperature-responsive imprinted porous material whose adsorption behavior was highly effected by both the imprinted cavities situation and the temperature responsive behaviors. The surface area of the ST after calcination have be measured for better understanding of adsorption mechanism of heavy metals by using N₂ adsorption-desorption isotherm. The surface areas of ST < ST-300 < ST-450 < ST-600 < ST-750 were 427.0, 462.3, 669.4, 1275.1 and 1589.6 m² g⁻¹, respectively, which has increased with the activation temperature increasing. The Langmuir model is the basic assumption

that monolayer adsorption occurs on the surface within the sorbent of a finite number of specific homogeneous sites. The adsorption sites were assumed to be energetically equivalent, as well as distant from each other, so that no interaction existed between the adjacent adsorbed molecules. Our experimental data indicate that the removal of Cd(II) with ST, ST-300, ST-450, ST-600, and ST-750 as adsorbents predominantly conforms to the monolayer adsorption. The mineral content and porous structures of the ST after thermal activation may contribute to the higher adsorption capacity for Cd(II). It is also presumed that all binding sites on the sorbent surface are free sites that are ready to accept the sorbent from solution.

3.5. Adsorption mechanism

In order to determine the chemical environment and microstructure of ST after Cd(II) adsorption, TEM and EDX measures have been performed with the results exhibited in Fig. 6. The peak of Cd elements can be clearly observed in Fig. 6(a1) and 6(a2). In order to further analyze the distribution of Cd element in the sample, the EDX analysis was conducted in the middle and marginal regions of the Fig. 6(a), as shown in Fig. 6(a1) and 6(a2), respectively. As can be seen, the peak of the Cd element in Fig. 6(a1) is lower than Fig. 6(a2). This means that the content of Cd in the peripheral region was greater than that in the middle region on the ST after the adsorption of Cd(II). The adsorbed Cd mainly exists on the surface of the sample rather than the interior. As shown in Fig. 6(b), the crystal particle with irregular distribution can be seen explicitly in the amorphous SiO₂. In order to further understand the microstructure and morphology of the crystal particles, the depth magnification and diffraction pattern of the randomly selected crystal particles were analyzed. The results are shown in Fig. 6(b1) and 6(b2). As can be seen in Fig. 6(b1), the crystal particle with size



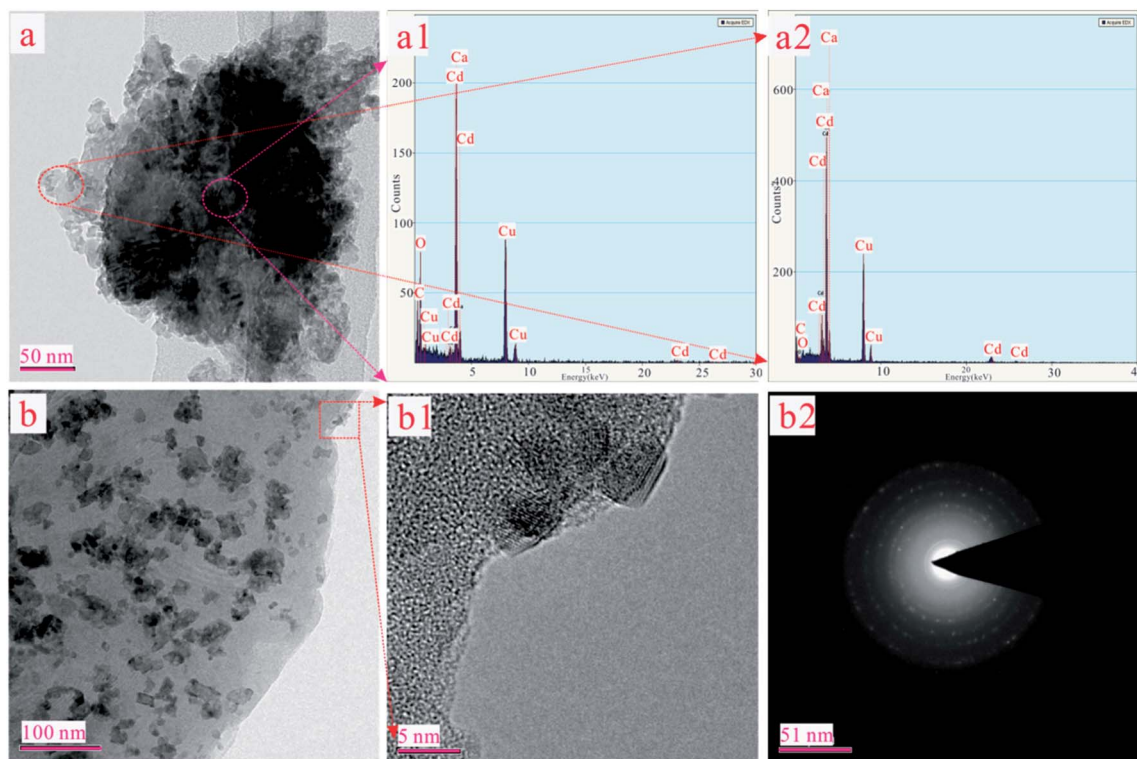


Fig. 6 (a) TEM images of ST-750 after the adsorption of Cd(II). (a1 and a2) Corresponding EDX elemental mapping images of (a). (b) TEM image of silica nanosheet of ST-750 after the adsorption of Cd(II). (b1) Magnified view of the red square region in (b). (b2) The diffraction pattern of (b1).

of about 5 nm was embedded onto the surface of sample. And there is an outline in the halo of the diffraction pattern as presented in Fig. 6(b2). It is suspected that CdCO_3 may be generated on the SiO_2 surface of the ST.

In addition, the XRD patterns of the different ST samples after adsorbed Cd(II) were given in Fig. 7. As shown in Fig. 7(a), the ST, ST-600 and ST(SD)-750 after adsorption of Cd(II) have the broadly consistent diffraction peaks related to the (012), (104), (006), (110), (113), (202), (018) (024), (112), (119), (300) planes contributed to calcite (PDF 05-0586[#]) and (100), (011) planes (PDF 85-0794[#]) contributed to silica. By carefully analyzing the Fig. 7(a) and enlarging it into Fig. 7(b), the XRD patterns of the

samples after Cd(II) ion adsorption did change slightly. For the sake of convenience, these areas have been marked as S1, S2, S3, and S4 regions in Fig. 7(b). As can be seen, the diffraction peaks of 20.87° (2θ) and 28.31° (2θ) disappeared ascribed to SiO_2 (PDF 85-0794[#]) in the region of S1, S3. The diffraction peaks of 24.45° (2θ) disappeared ascribed to calcite (PDF 03-0612[#]) in the region of S2. The peak width of 30.5° (2θ) gets broaden, indicating that the structure of ST has change due to the more Cd(II) adsorbed in the region of S4. The result means that thermal activation of the ST benefits of the adsorption of Cd(II).

XPS analyses were carried out to further investigate the adsorbent surface properties and the Cd(II) adsorption

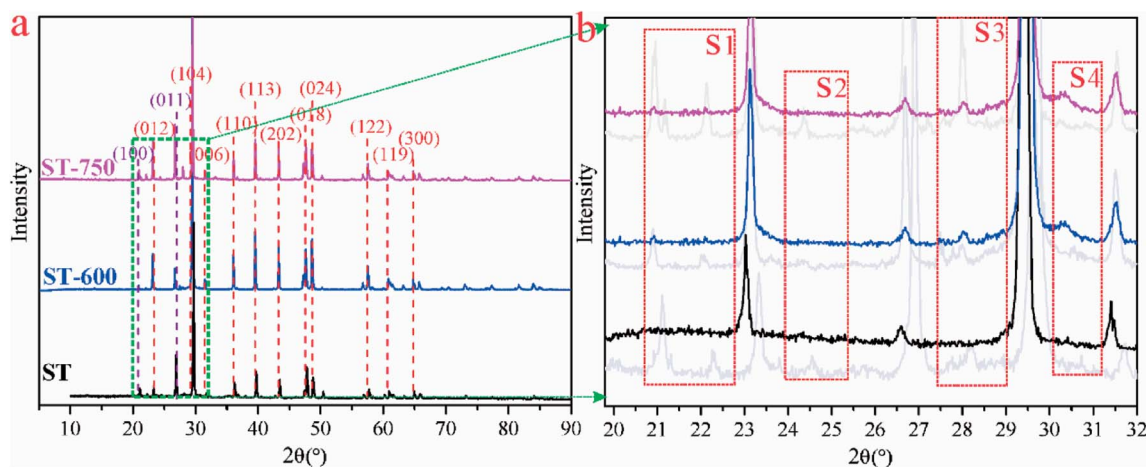


Fig. 7 (a) XRD patterns for ST, ST-600 and ST-750 after adsorption of Cd(II). (b) Magnified view of the green square region in (a).



mechanism. The relevant results of the ST and ST-750 after adsorption of Cd(II) were shown in Fig. 8. The peaks of Cd 3d distinctly appear in Fig. 8(a). It proved that the Cd(II) ion was successfully adsorbed into the adsorbent, which is consistent with the results of XRD and TEM. As can be seen in Fig. 8(b), there were C–O, C–C, C=C and CO_3^{2-} in the adsorbent after adsorption of Cd(II). As shown in Fig. 8(c), two peaks of the ST after adsorption of Cd(II) were varying that is for CdO (404.4 eV) and for Cd(OH)₂ (405.1 eV), which could be assigned to CdCO₃ and Cd(OH)₂. As can be seen in Fig. 8(d), three peaks of the ST-750 after adsorption of Cd(II) were varying that is for CdO (404.4 eV), for Cd(OH)₂ (405.1 eV), for Mont Cd (406.7 eV), which could be assigned to CdCO₃, Cd(OH)₂ and Cd(HCO₃)₂. The above peaks indicated that Cd(II) on the surface of ST and ST-750 after adsorption of Cd(II) was present as CdCO₃ (54.44%), Cd(OH)₂ (45.56%) and CdCO₃ (39.41%), Cd(OH)₂ (29.54%), Cd(HCO₃)₂ (31.05%), respectively. This indicated the adsorption of Cd(II) on the natural ST could be ascribed to the precipitation of CdCO₃ and Cd(OH)₂. Then, the adsorption of Cd(II) on the ST after thermal activation could be ascribed to the precipitation of CdCO₃, Cd(OH)₂ and Cd(HCO₃)₂. Combined with the results of TEM, it can be speculated that cadmium species were primarily

in the crystalline CdCO₃ precipitation form on all the samples after Cd(II) adsorbed. Moreover, the peak area corresponding to CdCO₃ was higher than that attributed to Cd(OH)₂ and Cd(HCO₃)₂. Generally, the adsorption of Cd(II) on ST was primarily surface precipitation.

3.6. Competitive adsorption

To understand the competitive adsorption behavior between Cd(II) and Pb(II), the dynamic interaction of the heavy metal cations Pb(II) with adsorbent ST-750 is necessary. ST-750 was added as an initial solid adsorbent into an aqueous solution with a known Pb(II) concentration at 298.1 K. As can be observed in Fig. 9(a), the Pb(II) adsorption had similar tendencies with Cd(II) adsorption. The Pb(II) concentration first sharply increased in the first approximately 200 min and then was followed by a relatively slower process for adsorption. Approximately 300 min was needed for the 400 mg L⁻¹ Pb(II) aqueous solution. Additionally, the pseudo first-order kinetic model and pseudo second-order kinetic model were used to describe the kinetic adsorption of Pb(II) with the results plotted in Fig. 9(a). Obviously, the pseudo second-order kinetic model could better

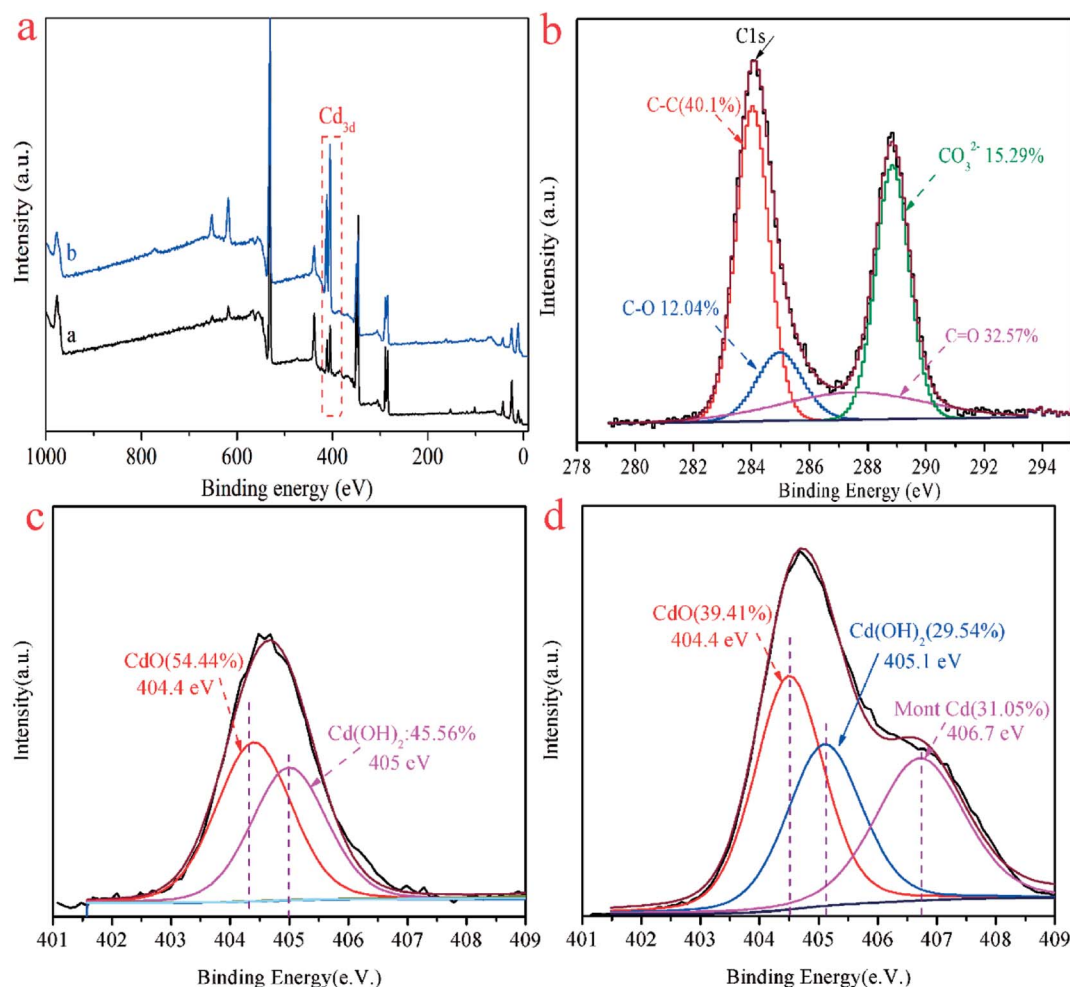


Fig. 8 (a) XPS spectra of ST and ST-750 after adsorption of Cd(II); (b) C 1s, C–C, C–O, C=C, and CO_3^{2-} spectra of ST after adsorption of Cd(II); (c) Cd 3d spectra of ST; (d) Cd 3d spectra of ST-750.



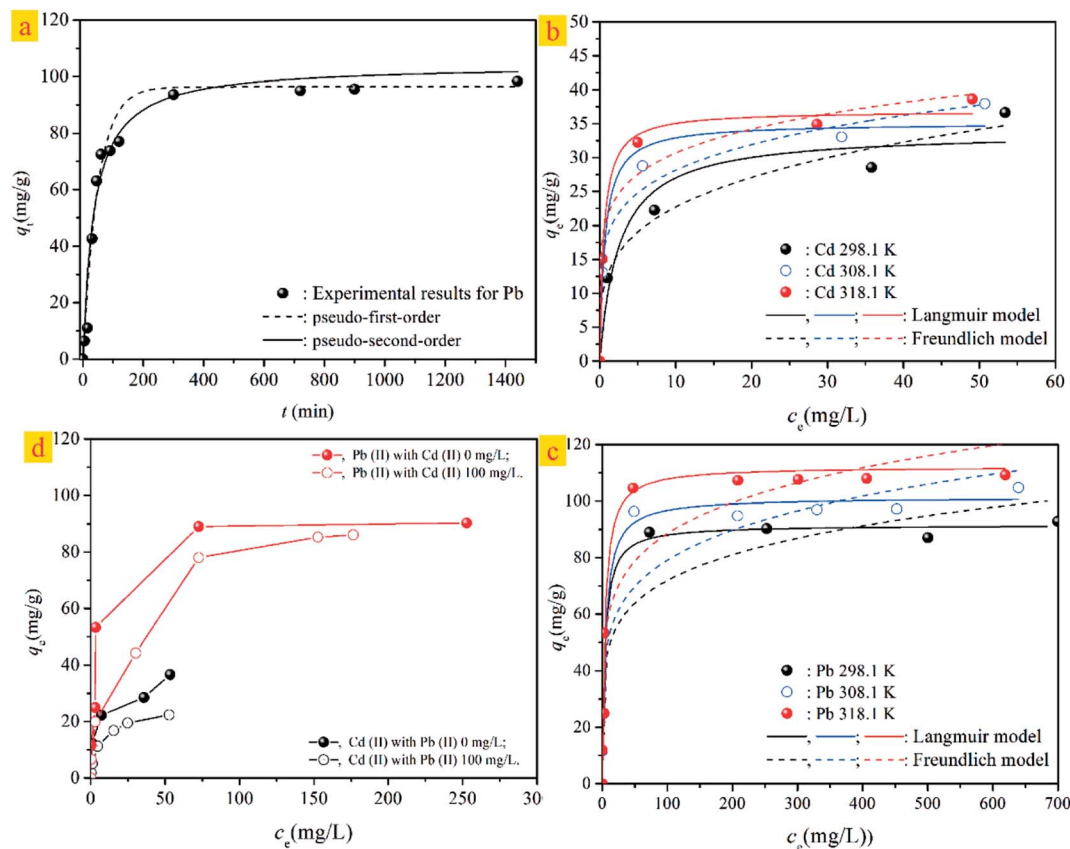


Fig. 9 (a) Kinetic models of ST-750 for Pb(II) adsorption. (b) Adsorption isotherms of Cd(II) adsorption on ST-750 as a function of temperature. (c) Adsorption isotherms of Pb(II) adsorption on ST-750 as a function of temperature. (d) Competitive adsorption between Cd(II) and Pb(II).

fit the experimental data indicating that the adsorption of Pb(II) occurs by chemical adsorption.

The adsorption isotherms of Cd(II) and Pb(II) with ST-750 as the adsorbent at $T = 298.1, 308.1$, and 318.1 K are shown in Fig. 9(b) and (c). The Langmuir and Freundlich models are applied to simulate and predict the experimental data with the model parameters tabulated in Table 4. Similar to the adsorption of Cd(II), the adsorption capacity of Pb(II) first increased and then remained unchanged at each temperature. The Langmuir model closely fits the adsorption of Cd(II) and Pb(II) with high correlation coefficients (R^2 , Table 4). Compared to Cd(II), the adsorption of Pb(II) is much higher; the maximum adsorption capacity (q_{\max}) values of Pb(II) adsorbed were 91.591 mg g^{-1} , $101.323 \text{ mg g}^{-1}$, and $112.192 \text{ mg g}^{-1}$ at 298.1 K, 308.1 K and 318.1 K. This finding can be explained by the hypothesis that the imprinted cavitation matches the template Pb(II) well in size along with coordination geometries, which benefit Pb(II) binding with the predetermined recognition sites. Pb(II) possesses a much lower heat of hydration than Cd(II), which may explain the higher adsorption capacity of Pb(II) than Cd(II).

The competitive adsorption between the Cd(II) and Pb(II) with ST-750 as the adsorbent has been investigated by studying the adsorption experiments on the influence of the Cd(II) initial concentration of 100 mg L^{-1} on the adsorption capacity for Pb(II) uptake and the influence of the Pb(II) initial concentration of 100 mg L^{-1} on the adsorption capacity for Cd(II) removal. The

experimental data for competitive adsorption are presented in Fig. 9(d). The adsorption capacity of Pb(II) is observably greater than that of Cd(II) accompanying binary aqueous solutions. Comparing the adsorption capacity for the ternary aqueous system with the binary aqueous system, the adsorption capacities of Cd(II) and Pb(II) both decrease with the addition of the other heavy metal cations. This indicates that the adsorption of the two ions is hindered by the competitive adsorption. Pb(II) is more responsive to the adsorbent than Cd(II), noting that adsorbents are more selective to Pb(II) than Cd(II). These results suggest that Pb(II) has a stronger ability to adsorb on the ST-750 compared to Cd(II). Thus, the adsorption active sites on the mineral surface are readily exchangeable. The model parameter K_L is related to the affinity between the adsorbent and the adsorbate, with larger K_L values associated with higher affinities. As shown in Table 3, the K_L values in contact with Pb(II) adsorption onto ST-750 were 0.2469 , 0.2105 and 0.2448 at 298.1 K, 308.1 K and 318.1 K. In contrast, the values for Cd(II) adsorption were 0.0757 , 0.1483 and 0.1243 at 298.1 K, 308.1 K and 318.1 K. Collectively, these data provide evidence that ST-750 has a higher affinity for Pb(II) than for Cd(II).

4. Conclusions

In summary, naturally porous fossil bryophyte has been modified by using a thermal activation technique for improving adsorption



capacity of heavy metals. The surface properties of natural straw tufa were first characterized by BET and TG-DSC. The BET results have ascertained natural mesoporous structures. The ST has specific surface area about $427.0 \text{ m}^2 \text{ g}^{-1}$ and a pore size at 11.77 nm. Then, X-ray diffraction (XRD) was used to characterize the phase composition of the ST. The ST was primarily composed of calcite and SiO_2 , which was further supported by the result of XRF. The ST has been activated thermally at 300, 450, 600 and 750°C . When the ST after thermal activation is further characterized using FT-IR, XRD, and SEM, the interface collapse and porous structural after thermal activation has occurred to form a coralliform and perforated structure. The thermal activated ST can be obtained with very good performance in terms of adsorption capacity and affinities to $\text{Cd}(\text{II})$. The adsorption capacity of the ST can be improved by thermal activation technology, and the capacity was strongly depend on the activation temperature, *i.e.* the adsorption capacity was increased in the order of $\text{ST} < \text{ST-300} < \text{ST-450} < \text{ST-600} < \text{ST-750}$, as that performed for ST-T. The maximum adsorption capacity of ST-750 is 33.81 mg g^{-1} . The adsorption kinetics can be better described by the pseudo-second-order kinetics model. The adsorption isotherm for $\text{Cd}(\text{II})$ onto different ST samples was well represented by the Langmuir model. By using TEM, XRD and XPS analysis, it proved that the CdCO_3 and $\text{Cd}(\text{OH})_2$ have generated on the surface of the calcareous tufa. The mechanisms of $\text{Cd}(\text{II})$ adsorption onto the calcareous tufa before and after thermal activation could be attributed to ion-exchange, surface complexation, and surface precipitation. Finally, through studying competitive adsorption experiment for $\text{Cd}(\text{II})$ and $\text{Pb}(\text{II})$, the adsorption of the two ions is hindered and the adsorption active sites on the mineral surface are readily exchangeable.

Conflicts of interest

There are no conflicts of interest to declare.

Acknowledgements

The authors gratefully acknowledge the financial support of the National Natural Science Foundation of China (Grant No: 21607176), the Natural Science Foundation of Hunan Province, China (Grant No. 2017JJ3516), the Research Foundation of the Education Bureau of Hunan Province, China (Grant No. 16B274), the Open Fund for Key Discipline of Forestry of Central South University of Forestry and Technology (Grant No. 2016ZD11), and the Youth Scientific Research Foundation of Central South University of Forestry and Technology (104|0329).

References

- 1 A. Benettayeb, E. Guibal, A. Morsli and R. Kessas, *Chem. Eng. J.*, 2017, **316**, 704–714.
- 2 Q. Q. Zuo, C. Chen, H. J. Cui and M. L. Fu, *RSC Adv.*, 2017, **7**, 16238–16243; J. Y. He, Y. L. Li, C. M. Wang, K. S. Zhang, D. Y. Lin, L. T. Kong and J. H. Liu, *Appl. Surf. Sci.*, 2017, **426**, 29–39.
- 3 S. Q. Xiong, J. C. Xu, F. Z. Xie, X. H. Hu, G. H. Gong, Z. Y. Wu and L. M. Yao, *Chem. Eng. J.*, 2017, **316**, 383–392.
- 4 P. S. De Velasco-Maldonado, V. Hernández-Montoya, M. A. Montes-Morán, N. A.-R. Vázquez and M. A. Pérez-Cruz, *Appl. Surf. Sci.*, 2018, **434**, 1193–1199.
- 5 E. Da'na, *Microporous Mesoporous Mater.*, 2017, **247**, 145–147.
- 6 W. W. Gong, Y. J. Yu, G. Liang, X. H. Liu, B. S. Cui, J. H. Bai and P. Han, *Colloids Surf., A*, 2018, **538**, 460–466.
- 7 H. Demey, T. Vincent and E. Guibal, *Chem. Eng. J.*, 2018, **332**, 582–595.
- 8 D. Kavak, *Desalin. Water Treat.*, 2013, **51**, 1720–1726.
- 9 H. Yin and J. Zhu, *Chem. Eng. J.*, 2016, **285**, 112–120.
- 10 S. Heuss-Assbichler, M. John, D. Klapper, U. W. Blass and G. Kochetov, *J. Environ. Manage.*, 2016, **181**, 1–7.
- 11 J. Wang, W. T. Zhang, X. Y. Yue, Q. F. Yang, F. B. Liu, Y. R. Wang, D. H. Zhang, Z. H. Li and J. L. Wang, *J. Mater. Chem. A*, 2016, **4**, 3893–3900.
- 12 C. W. Wong, J. P. Barford, G. Chen and G. McKay, *J. Environ. Chem. Eng.*, 2014, **2**, 698–707.
- 13 M. Benamor, Z. Bouariche, T. Belaid and M. T. Draa, *Sep. Purif. Technol.*, 2008, **59**, 74–84.
- 14 O. Arar, *Desalin. Water Treat.*, 2014, **52**, 3197–3205.
- 15 M. C. Revathi, A. Basha and M. Velan, *Desalin. Water Treat.*, 2016, **57**, 20350–20367.
- 16 M. Garmsiri and H. R. Mortaheb, *Chem. Eng. J.*, 2015, **264**, 241–250.
- 17 P. Otrembska and J. Gega, *Sep. Sci. Technol.*, 2016, **51**, 2675–2680.
- 18 J. Kheriji, D. Tabassi and B. Hamrouni, *Water Sci. Technol.*, 2015, **72**, 1206–1216.
- 19 H. Duan, S. Wang, X. Yang, X. Yuan, Q. Zhang, Z. Huang and H. Guo, *Chem. Eng. Res. Des.*, 2017, **117**, 460–471.
- 20 A. Labidi, A. M. Salaberria, S. C. M. Fernandes, J. Labidi and M. Abderrabba, *J. Taiwan Inst. Chem. Eng.*, 2016, **65**, 140–148.
- 21 M. Mushtaq, H. N. Bhatti, M. Iqbal and S. Noreen, *J. Environ. Manage.*, 2016, **176**, 21–33.
- 22 Z. S. Chen, G. J. Lee and J. C. Liu, *Chemosphere*, 2000, **41**, 235–242.
- 23 W. Y. Shi, H. Li, S. Du, K. B. Wang and H. B. Shao, *Appl. Clay Sci.*, 2013, **85**, 103–108.
- 24 C. Y. Cao, C. H. Liang, Y. Yin and L. Y. Du, *J. Hazard. Mater.*, 2017, **329**, 222–229.
- 25 M. J. Wu, J. Zhang, Y. Q. Peng, J. Z. Zhou, X. X. Ruan, J. Y. Liu, Q. Liu, Y. F. Xi, R. Frost and G. G. Qian, *Microporous Mesoporous Mater.*, 2017, **242**, 182–189.
- 26 R. Krebs, S. K. Gupta, G. Furrer and R. Schulz, *Water, Air, Soil Pollut.*, 1999, **115**, 465–479.
- 27 E. Lombi, F. J. Zhao, G. Zhang, B. Sun, W. Fitz, H. Zhang and S. P. McGrath, *Environ. Pollut.*, 2002, **118**, 435–443.
- 28 C. Keller, M. Marchetti, L. Rossi and N. Lugon-Moulin, *Plant Soil*, 2005, **276**, 69–84.
- 29 Y. Du, F. Lian and L. Y. Zhu, *Environ. Pollut.*, 2011, **159**, 1763–1768.
- 30 C. A. Flemming, F. G. Ferris, T. J. Bevaridge and G. W. Bailey, *Appl. Environ. Microbiol.*, 1990, **56**, 3191–3203.



- 31 R. Celis, M. C. Hermosin and J. Cornejo, *Environ. Sci. Technol.*, 2000, **34**, 4593–4599.
- 32 H. Ni, Y. L. Li, R. P. Cui, Y. Lu and G. D. Yang, *J. Environ. Eng.*, 2016, **6**, 3077–3083.
- 33 S. Y. Hao, A. Verlotta, P. Aprea, F. Pepe, D. Caputo and W. D. Zhu, *Microporous Mesoporous Mater.*, 2016, **236**, 250–259.
- 34 G. Li, B. D. Wang, Q. Sun, W. Q. Xu and Y. F. Han, *Microporous Mesoporous Mater.*, 2017, **252**, 105–115.
- 35 M. Liu, Y. Wang, L. Chen, Y. Zhang and Z. Lin, *ACS Appl. Mater. Interfaces*, 2015, **7**, 7961–7969.
- 36 W. L. Wang, D. W. Zeng and Q. Y. Chen, *Chem. Eng. Sci.*, 2013, **101**, 120–129.
- 37 J. Wen, Z. L. Peng, Y. G. Liu, Y. Fang, G. M. Zeng and S. Y. Zhang, *J. Soils Sediments*, 2018, **18**, 323–332.
- 38 C. Y. Cao, C. H. Liang, Y. Yin and L. Y. Du, *J. Hazard. Mater.*, 2017, **329**, 222–229.

